Adhesion-Induced Instability Patterns in Thin Confined Elastic Film

Animangsu Ghatak and Manoj K. Chaudhury*

Department of Chemical Engineering, Lehigh University, Iacocca Hall, 111 Research Drive, Bethlehem, Pennsylvania 18015-4791

Adhesion-induced instability has been observed at the interface of a flexible plate and a thin elastic film bonded to a rigid substrate. The surface of the confined film develops undulations almost instantaneously, and instability patterns appear in the form of fingers or bubbles at the interface. The characteristic wavelengths of these instabilities remain independent of all material and geometrical properties of the system except the thickness of the film. These observations contrast sharply with the Saffman–Taylor-type phenomenon in which the length scale of the instability patterns depends on the viscous and surface tension forces in addition to the thickness of the liquid film. The analogy between the phenomenon reported here and the Rayleigh–Kelvin instability with curved liquid menisci is more pronounced, as, in both cases, surface force triggers the instability while not determining its wavelength. The instability also throws light on cavitation phenomena in confined adhesive layers.

Introduction

Hydrodynamic-force-driven nonequilibrium systems give rise to many different instability patterns ranging from simple fingerlike[1-3] to highly exotic dendritic[4-6] structures. The simplest of these various pattern-forming systems is a Hele–Shaw cell, where a low-viscosity fluid displaces a high-viscosity one between two parallel plates, leading to a fingering instability in the moving interface. This phenomenon is known as the Saffman–Taylor instability,[1] where the characteristic wavelength (λ) of the fingering pattern is determined by the balance of two counteracting forces: the negative pressure gradient and the Laplace pressure. λ increases linearly with the thickness of the confined space and inversely with the capillary number as $\lambda \sim h/\sqrt{Ca}$. A rather intriguing result is obtained with two immiscible liquids with a very high viscosity ratio[5] (10^2–10^4) or in plug-flow conditions with two miscible fluids[7,8] in a Hele–Shaw cell. Here, although the negative hydrostatic pressure gradient triggers the instability, the interfacial tension is too low to provide any kind of stability to the system. The stability[7] in this case is provided by viscous dissipation between the fingers. As a result, the wavelength of the instability simply varies linearly with the thickness of the confined film as $\lambda = 4.0h$, the result being independent of the velocity and other material properties of the system.

Whereas simple viscous systems are now fairly well understood, difficulty arises in understanding the phenomena in viscoelastic systems because of their simultaneous elastic and viscous characters. A common approach toward understanding viscoelastic pattern for-

mation has been to introduce a switching criterion, e.g., the nondimensional Deborah number[9,10] (*De*). At low Deborah numbers ($De \ll 1$), the hydrodynamic forces dominate pattern formation, whereas at high Deborah numbers ($De \gg 1$), systems behave as elastic solids. Although this approach provides an easy crossover from viscous to viscoelastic systems, an important missing link in this context has been a systematic study of pattern formation in purely elastic systems in comparable geometries. For example, Lemire et al.[11] reported that the fractal dimensions of the instability patterns obtained by injecting a low-viscosity liquid into a viscoelastic medium[12,13] remain unaffected by the interfacial tension; it merely increases the size of the pattern. It is not readily obvious why the interfacial tension does not influence the fractal dimensions of patterns in viscoelastic fracture. In another example, when a pressure-sensitive adhesive is peeled from a solid substrate, an instability develops at the contact line, and fingerlike patterns evolve.[14,15] Although these fingers look very similar to those observed in viscous systems, they are different, because the characteristic spacing between the viscoelastic fingers remains independent of the velocity of peeling, unlike the behavior of the viscous counterpart. In the absence of sufficient knowledge about purely elastic system, it has been argued[16] that this instability in viscoelastic adhesives parallels the Saffman–Taylor behavior[1] in viscous systems. The velocity independence of instability was attributed to the non-Newtonian character of the viscoelastic liquid. Similar questions arise in the context of cavitation or bubble formation, which occurs when a rigid indenter

* To whom correspondence should be addressed.

(1) Saffman, P. G.; Taylor, G. I. *Proc. R. Soc. London* **1958,** *A245,* 312.
(2) Homsy, G. M. *Annu. Rev. Fluid Mech.* **1981,** *19,* 271
(3) Paterson, L. *J. Fluid Mech.* **1981,** *113,* 513.
(4) Nittmann, J.; Daccord, G.; Stanley, H. E. *Nature* **1985,** *314,* 141.
(5) Daccord, G.; Nittmann, J.; Stanley, H. E. *Phys. Rev. Lett.* **1986,** *56,* 336.
(6) Van Damme, H.; Obrecht, F.; Levitz, P.; Gatineau, L.; Laroche, C. *Nature* **1986,** *320,* 731.
(7) Paterson, L. *Phys. Fluids* **1985,** *28* (1), 26.
(8) Van Damme, H.; Alsac, E.; Laroche, C.; Gatineau, L. *Europhys. Lett.* **1988,** *5* (1), 25.

(9) Reiner, M. *Phys. Today* **1964,** *17,* 62.
(10) McKinley, G. H. Dynamics of Complex Fluids. In *Proceedings of the Royal Society/Unilever Indo-UK Forum*; Adams, M. Ed.; ICL Press: London, 1998.
(11) Lemaire, E.; Levitz, P.; Daccord, G.; Van Damme, H. *Phys. Rev. Lett.* **1991,** *67,* 2009.
(12) Van Damme, H.; Laroche, C.; Gatineau, L. *Rev. Phys. Appl. (Paris)* **1987,** *22,* 141.
(13) Van Damme, H.; Laroche, C.; Gatineau, L.; Levitz, P. *J. Phys. (Paris)* **1987,** *48,* 1221.
(14) Urahama, Y. *J. Adhes.* **1989,** *31,* 47.
(15) Newby, Bi-min Zhang; Chaudhury, M. K.; Brown H. R. *Science* **1995,** *269,* 1407.
(16) Fields, R. J.; Ashby, M. F. *Philos. Mag.* **1976,** *33,* 33.

is detached from a layer of viscoelastic adhesive. Cavitation in viscoelastic rubber was first observed in the experiments of Gent et al.[17−19] and Kaelble[20] and was recently seen in the experiments of Pond[21] and Creton et al.[22,23] It has been argued[18,22−25] that cavitation and bubble formation occur at the interface as a result of the presence of microscopic and macroscopic air bubbles at surface defects. Under a tensile stress, negative pressure develops in the air bubbles, and they expand to form cavities. Questions arise as to whether there is any characteristic length scale for the appearance of bubbles and whether the surface roughness determines that length scale. Because the wavelength reflects the underlying physics of the phenomenon, it is imperative to carry out a detailed analysis of the patterns of bubble formation in cavitation experiments. A simple beginning in this case could be to study the patterns of cavitation in a purely elastic system, in a geometry similar to that of the classical probe tack experiment.

Most notable among the surface and interfacial instabilities in a confined elastic film are the Schallamach waves,[26] which are observed in sliding experiments of a soft rubber indenter on a hard surface and vice versa. "Waves of detachment" originate at the front of the contact area and move rapidly to the rear at a speed much higher than the sliding velocity of the indenter. These waves have been understood to be elastic instabilities caused by buckling of the rubber by tangential compressive stresses present in that area. However, stationary instability waves in the shape of a "V" were first observed by Lake et al.[27] during the peeling of a rubber strip from glass at a low peel angle. Although Lake et al.[27] understood these instabilities to be elastic in nature, they performed no systematic study to analyze the effects of different material and geometrical properties of the system on the morphology of the waves and thus on the overall energetics of the system. Recently, Shull et al.[28] reported fingering instabilities in elastic gel subjected to tensile stress and explained them to be triggered by negative hydrostatic stress very similar to the Saffman−Taylor instability in viscous systems.[1] Recently, we reported a new kind of instability that was observed in experiments[29] with confined thin (length parallel to the plane of the film much greater than the film thickness) films of purely elastic material. In these experiment, a flexible plate is brought into contact with a thin elastic film bonded to a rigid substrate in the geometry of a classical peel experiment. The two surfaces remain in contact everywhere except close to the crack tip, where the contact line breaks into uniformly spaced fingers. The space between the fingers increases linearly with the thickness of the film (h) as $\lambda = 4h$ but remains independent of all other material properties. The length of the fingers, however, increases with increasing rigidity of the plates. For highly rigid plates, the 1-D fingers degenerate into 2-D isotropic

patterns. Mönch et al.[30] also reported a similar experiment with rigid plates that led to isotropic instability patterns in the contact area, with the result $\lambda = 3h$. A plane strain model proposed by Mönch and Herminghaus[30] as well as by Shenoy and Sharma[29,31] captured the essential physics of this phenomenon and predicted correctly the relation $\lambda = 3h$ observed in the isotropic situation. The model attributed the instability phenomenon to the competition between the distance-dependent adhesion forces between the two surfaces and the elastic restoring forces in the film. At a critical separation distance between the two surfaces, where the gradient of the adhesion force becomes greater than the ratio of the modulus to the thickness of the film, instabilities develop on the film surface.

The objective of the current study is to expand our knowledge on instability pattern formation in purely elastic systems. To this end, we have performed contact mechanics experiments similar to the peel experiment in different geometries and have investigated the morphological features of the instabilities. We also extend our discussion to the phenomenon of cavitation or bubble formation in confined elastic systems.

Experimental Section

Materials. The glass slides (Corning microslides) and cover slips (Corning cover plates) used for these experiments were obtained from Fisher Scientific. The glass slides were cleaned in a Harrick plasma cleaner (model PDC-23G, 100 W) before surface treatment. The material for film preperation, i.e., vinyl-end-capped poly(dimethylsiloxane) oligomers of different chain lengths, platinum catalyst, and the methylhydrogen siloxane cross-linker, were obtained as gifts from Dow Corning Corp., Midland, MI. Two sets of filler gauges of various thicknesses were required for making the films of controlled thickness; these were purchased from a local auto-parts shop. The instability patterns were observed with a Nicon Diaphot inverted microscope equipped with a CCD camera and a video recorder.

Methods. Preparation of Glass Plates and Glass Disks. The rigid glass slides (Corning microslides) and the flexible cover plates (Corning cover plates) used in these experiments were thoroughly cleaned by immersing them in hot piranha solution for 30 min, rinsed with deionized water, and blow-dried in pure nitrogen gas. The glass slides were further cleaned in oxygen plasma at 2.0×10^{-4} atm for 30 s. One set of these glass slides was used for cross-linking the polymer onto the slide surface. The other set of glass slides and the flexible plates were coated with an self-assembled monolayer (SAM) of hexadecyl trichlorosilane (HC). Details of the monolayer formation process are described in ref 32.

The flexural rigidity[33] (D) of the cover slips was measured by a cantilever beam experiment in which one end of the cover plate was fixed on a rigid support while the other end was loaded with known dead weights (P). The displacement (Δ) of this end was measured, and the flexural rigidity was calculated using the equation[34]

$$D = \frac{PL^3}{6\Delta b} \tag{1}$$

where L is the length of the glass plate and b is its width. For some experiments, cover plates with larger flexural rigidities were prepared by gluing together two or more cover slips using Sylgard-184 (Dow Corning) elastomer and cross-linking the polymer at 80° C for 1 h.

(17) Gent, A. N.; Lindley, P. B. *Proc. R. Soc. London* **1959**, *A249*, 195.
(18) Gent, A. N.; Tompkins, D. A. *J. Appl. Phys.* **1969**, *40* (6), 2520.
(19) Gent, A. N.; Tompkins, D. *J. Polym. Sci. A2* **1969**, *7*, 1483.
(20) Kaelble, D. H. *Trans. Soc. Rheol.* **1971**, *15*, 275.
(21) Pond, T. J. *J. Nat. Rubber Res.* **1993**, *8* (2), 83.
(22) Lakrut, H.; Sergot P.; Creton, C. *J. Adhes.* **1999**, *69*, 307 and references therein.
(23) Creton, C.; Lakrut, H. *J. Polym. Sci. B: Polym. Phys.* **2000**, *38*, 965.
(24) Lindsey, G. H. *J. Appl. Phys.* **1967**, *38* (12), 4843.
(25) Gay, C.; Leibler, L. *Phys. Rev. Lett.* **1999**, *82*, 936.
(26) Schallamach, A. *Wear* **1971**, *17*, 301.
(27) Lake G. J.; Stevenson, A. *J. Adhes.* **1981**, *12*, 13.
(28) Shull, K. R.; Flanigan, C. M.; Crosby, A. J. *Phys. Rev. Lett.* **2000**, *84*, 3057.
(29) Ghatak, A.; Chaudhury, M. K.; Shenoy, V.; Sharma, A. *Phys. Rev. Lett.* **2000**, *85*, 4329.

(30) Mönch, W.; Herminghaus, S. *Europhys. Lett.* **2001**, *53*, 525.
(31) Shenoy, V.; Sharma, A. *Phys. Rev. Lett.* **2001**, *86*, 119.
(32) Chaudhury, M. K.; Whitesides, G. M. *Langmuir* **1991**, *7*, 1013.
(33) Flexural rigidity[34] $D = \mu' t^3/6(1 − \nu)$, where μ' is the shear modulus of the cover plate, ν is its Poisson's ratio, and t is its thickness.
(34) Landau, L. D.; Lifshitz, E. M. *Theory of Elasticity*, 3rd revised ed.; Course of Theoretical Physics; Pergamon Press: New York, 1986; Vol. VII.
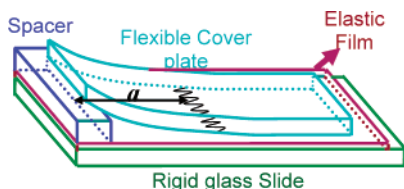
Figure 1. Schematic of the experiments in which a flexible glass plate is brought into contact with an elastomeric film in the configuration of a cantilever beam. The film remains strongly adhered to a rigid substrate. A spacer is inserted into the opening of the crack. Instabilities in the form of uniformly shaped and uniformly spaced fingers appear at the contact line (Figure 3). The figure is not drawn to scale.

Borosilicate glass disks of 8-mm diameter were obtained from Swift Glass Inc. One of the disks was cleaned and coated with a SAM of HC by the above method. The second was used for the grafting of long-chain PDMS [$HSi(CH_3)_2(OSi(CH_3)_2)_n(CH_2)_3CH_3$] molecules of molecular weight $M = 20\,000$. Details of the grafting method are described in ref 35.

Preparation of Thin Films. Cross-linked elastomeric films of PDMS were prepared between two microscope glass slides by platinum-catalyzed hydrosilation of vinyl-end-capped dimethylsiloxane oligomers to methylhydrogensiloxane cross-linker. The glass slides (Corning microslides) were kept separated by spacers of known heights (40–2000 μm). One of the glass slides was coated with a SAM, which ensured its removal from the elastomeric film after it was cross-linked. The film, however, remained strongly adhered to the untreated glass slide. Oligomers of different molecular weights (2000–50 000) were used to prepare cross-linked networks of different elastic moduli (0.2–6.0 MPa).

A dynamic mechanical analysis of these networks in a frequency sweep at ambient temperature (25 °C) showed that the loss modulus (μ'') was at least 2 orders of magnitude lower than the storage modulus (μ'). This result indicated that the networks are primarily elastic with negligible viscosity effects.[36] The same conclusion was reached in Johnson–Kendall–Roberts (JKR)[37] experiments in which hemispherical lenses of the same networks were brought into contact with a Si wafer coated with a self-assembled monolayer (SAM) of hexadecyl trichlorosilane molecules. The loading data at a particular contact diameter remained unchanged with respect to time, which again showed that the cross-linked networks did not have any dynamic rheological property.

Contact Experiments. A schematic of the experimental setup is shown in Figure 1, in which a flexible glass plate is brought into contact with the PDMS film in the form of a cantilever, which was loaded by means of a spacer inserted in the opening of the crack. The experiment has the advantage of a simple geometry as in the classical peel experiment.[38–40] It also matches the geometry of Hele–Shaw cells with lifting plates.[16,41,42] Cover plates with different flexural rigidities ($D = 0.02$–0.6 N·m) could be subjected to both crack-opening and crack-closing experiments with or without a spacer. In crack-opening mode, an external load is applied to lift the cover plate so that the contact line moves away from the spacer. In crack-closing mode, the plate is brought into contact with the film by the internal force of adhesion[43] (40 mJ/m²). In this case, the contact line moves toward the spacer and comes to an equilibrium position.

The experiment could also be performed in a radially symmetric geometry (Figure 2), in which a small glass sphere (~50–100 μm

(35) She, H.; Malotky, D.; Chaudhury, M. K. *Langmuir* **1998**, *14*, 3090.
(36) Thanawala, S. K.; Chaudhury, M. K. *Langmuir* **2000**, *16*, 1256.
(37) Johnson, K. L.; Kendall, K.; Roberts, A. D. *Proc. R. Soc. London* **1971**, *A324*, 301.
(38) Kaelble, D. H. *Trans. Soc. Rheol.* **1960**, *4*, 45.
(39) Kaelble, D. H. *Trans. Soc. Rheol.* **1965**, *9*, 135.
(40) Gent, A. N.; Hamed, G. R. *J. Adhes.* **1975**, *7*, 91.
(41) Ben-Jacob, E.; Godbey, R.; Goldenfeld, N. D.; Koplik, J.; Levine, H.; Mueller, T.; Sander, L. M. *Phys. Rev. Lett.* **1985**, *55*, 1315.
(42) Zhang, S.-Z.; Louis, E.; Pla, O.; Guinea, F. *Eur. Phys. J. B* **1998**, *1*, 123.
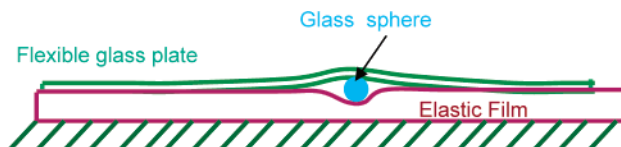(43) Obtained from JKR[37] experiments.

Figure 2. Schematic of the experiments in which a glass sphere is used as a spacer and a glass cover plate is brought into contact with the film. Here, too, the elastic film remains strongly adhered to a rigid substrate. Instabilities appear in the form of circular and elongated fingers along a ring with the glass sphere at its center (Figure 4). The figure is not drawn to scale.
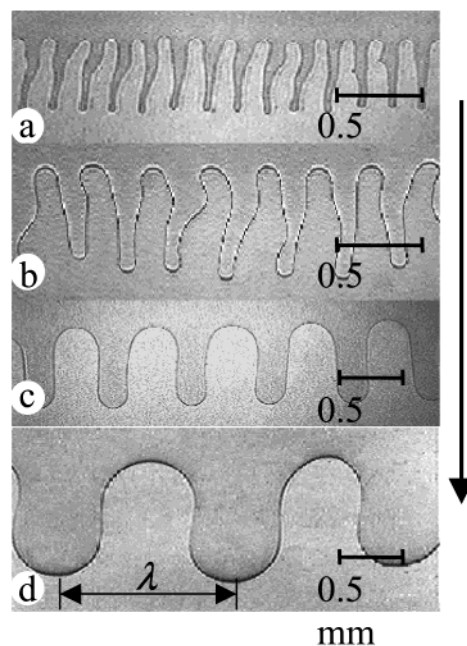

Figure 3. Video micrographs of instabilities triggered by forces of adhesion in the experiments depicted Figure 1. Glass plates of different flexural rigidities are brought into contact with elastomeric films of various thicknesses and shear moduli. Micrograph a corresponds to an elastic film of thickness $h = 40$ μm and shear modulus $\mu = 2.0$ MPa and a cover glass of flexural rigidity $D = 0.02$ N·m; micrograph b corresponds to $h = 80$ μm, $\mu = 0.25$ MPa, and $D = 0.02$ N·m; micrograph c corresponds to $h = 160$ μm, $\mu = 1.0$ MPa, and $D = 0.2$ N·m; and micrograph d corresponds to $h = 350$ μm, $\mu = 0.25$ MPa, and $D = 0.4$ N·m. The arrow shows the direction in which the crack opens.

in diameter) is placed on the film as a spacer. The flexible plate is brought into contact with the film from the top. Here, too, the glass plate bends and makes a circular contact, which remains stationary by the balance of the bending stress of the flexible plate and the adhesion stress at the interface. This arrangement corresponds to a radial Hele–Shaw cell[3,5] in a liquid system, in which a liquid between two parallel disks is displaced radially by pushing air through a hole at the center of one of the disks.

Results and Discussion

Instability Patterns. Figures 3 and 4 show video micrographs of the instabilities corresponding to the experiments depicted in Figures 1 and 2, respectively. The patterns evolve almost instantaneously when the flexible plate contacts films with thicknesses lower than a critical thickness (h_c). This critical thickness depends on the shear modulus (μ) of the film and the rigidity (D) of the cover plate. However, no undulation is observed when films with thicknesses greater than h_c are used. For $h < h_c$, the patterns appear and remain stable irrespective of whether the crack is opened, closed, or at rest. In other words, the formation of these fingers does not depend on
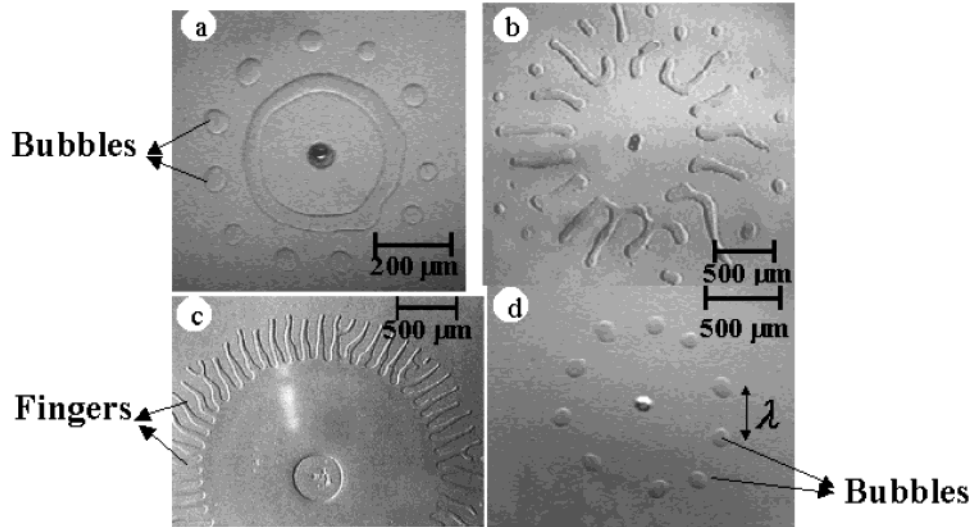
Figure 4. Video micrographs of instability patterns in the experiments depicted in Figure 3. A glass sphere, at the center of each image, is used as a spacer, and a glass cover plate with a rigidity (D) of 0.02 N·m is brought into contact with films of different shear moduli (μ) and thicknesses (h). Micrographs a and b correspond to $\mu = 0.25$ MPa and $h = 40$ μm and 80 μm, respectively. Micrographs c and d correspond to $\mu = 2.0$ MPa and $h = 40$ and 80 μm, respectively. The two surfaces are not in contact in regions where instability patterns are developed.

the velocity of the contact line unlike its counterpart in viscous systems.

In experiments of the type depicted in Figure 1, the crack front develops into wavy undulations, and well-shaped fingers with uniform spacing are observed. Micrographs a–d in Figure 3 correspond to films of increasing thickness (40–350 μm) and varying shear modulus ($\mu = 0.25$–2.0 MPa). The arrow indicates the direction in which the crack opens. The uniform shape of the fingers in these micrographs indicates that the normal stress distribution in the film along the direction of the contact line is uniform. The spacing between the fingers increases with the thickness of the film, but it does not depend on the flexural rigidity of the plate. However, for each film of a given modulus and thickness, instability does not develop if the upper plate is too flexible. For example, note micrograph 3d, in which a cover plate of flexural rigidity $D = 0.4$ N·m is brought into contact with a film of thickness 350 μm. No undulation is observed for this film if a more flexible plate (e.g., $D = 0.02$ N·m) is used. For the plate with $D = 0.2$ N·m (Figure 3c), the instability disappears if the film thickness exceeds 330 μm. Experiments with films of different thicknesses and elastic moduli and cover plates of different rigidities indicate that the critical thickness (h_c) beyond which instability disappears varies linearly with $(D/\mu)^{1/3}$, as shown in Figure 5.

In experiments of the type depicted in Figure 2, films of two different thicknesses (40 and 80 μm) and shear moduli (0.25 and 2.0 MPa) were used, whereas the flexural rigidity of the cover plate were maintained at $D = 0.02$ N·m. Films of shear modulus $\mu = 0.25$ MPa are used in micrographs 4a and b corresponding to film thicknesses of 40 and 80 μm, respectively. In micrographs 4c and d, the elastic modulus of films was $\mu = 2.0$ MPa, and the film thicknesses were 40 and 80 μm, respectively. The results summarized in Figure 4 show that the instability patterns appear as equally spaced bubbles (Figure 4a and d), elongated fingers (Figure 4c), or broken fingers (Figure 4b) along a circular ring with the glass sphere at its center. The wavelength of the instability is measured by estimating the distance between these features along the ring.

An interesting aspect of the instability patterns in Figures 3 and 4 is the directionality of the waves. Whereas the waves in Figure 3 are formed along the contact line,
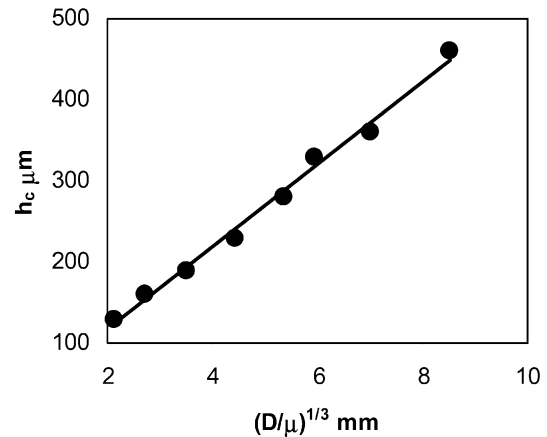

Figure 5. For every value of D and μ, there exists a critical thickness (h_c) of the film above which the instability disappears. Critical thickness data (h_c) obtained from experiments with films of different elastic moduli (μ) and cover plates of different flexural rigidities (D) scales nicely with the quantity $(D/\mu)^{1/3}$.

i.e., in the direction normal to crack propagation, the waves in Figure 4 appear along the circle of detachment. This spatial directionality makes this case different from the isotropic situation, where isotropic wave vectors appear throughout the contact area. These unidirectional waves are referred to as 1-D patterns in this paper.

Wavelength. The wavelengths of the instability patterns shown in Figures 3 and 4 remain independent of either the shear modulus (μ) of the film or the flexural rigidity[33] (D) of the plate, but they increase linearly with the thickness (h) of the film. The wavelengths obtained from numerous experiments as depicted in Figures 1 and 2 can be plotted on a single master curve (Figure 6) with the result $\lambda = 4h$. The wavelength does not even depend on the force of adhesion between the film and the contacting plate. This particular observation was made in experiments where the adhesion strength was enhanced by oxidizing the film in a plasma chamber and then bringing it into contact with a flexible plate in the geometry of Figure 1. The spacing between the fingers remained unaltered despite the considerable enhancement of the adhesion at the interface. This situation is somewhat
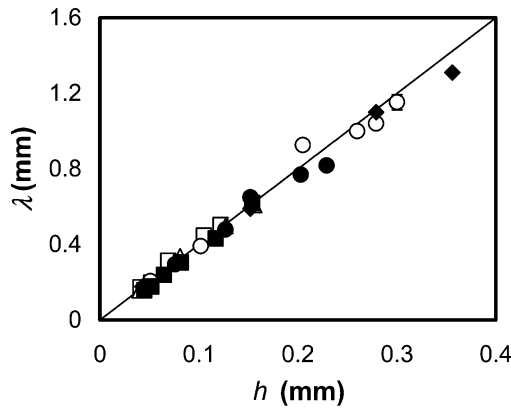
Figure 6. Wavelengths (λ) of instability patterns from the experiments depicted in Figures 1 and 2 increases linearly with the thickness (h) of the films. The wavelength, however, remains independent of both the elastic modulus of the elastomer and the rigidity of the glass plate. Symbols □, ○, and △ correspond to a cover glass plate of flexural rigidity $D = 0.02$ N·m against films of moduli (μ) 2.0, 1.0, and 0.25 MPa, respectively; ● corresponds to $D = 0.09$ N·m and $\mu = 0.25$ MPa; and ■ and ◆ correspond to $D = 0.4$ N·m and $\mu = 1.0$ and 0.25 MPa, respectively. Data from all experiments fall on a single straight line satisfying the relation $\lambda = 4h$.
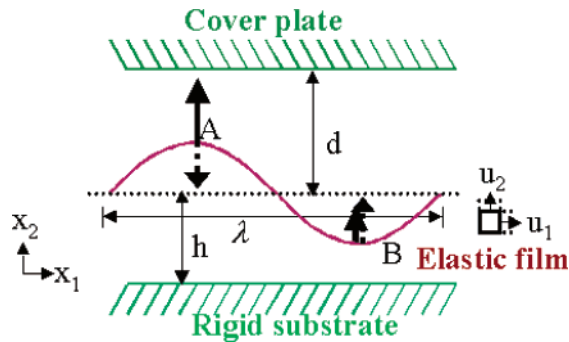

Figure 7. Schematic of a simple experiment in which a thin elastic film bonded to a rigid substrate is subjected to adhesion forces by being brought into contact with a rigid cover plate. The arrows indicate the forces acting on the film. The solid arrows represent attractive van der Waals forces, which tend to enhance any initial perturbation on the surface of the film, and the dashed arrows represent the elastic forces, which tend to inhibit the growth of instability.

similar to the classical Rayleigh–Kelvin instability[44] on a cylindrical liquid surface, which breaks up into liquid drops as a result of a gradient in the Laplace pressure. Although surface forces trigger the instability, the wavelength depends only on the diameter of the liquid cylinder ($\lambda = \pi d$) and not on its surface tension. The wavelength of the elastic instability also remains independent of the velocity of the moving contact line, in contrast to the classical Saffman–Taylor instability[1,2] with immiscible liquids. It remains unaltered irrespective of whether the crack opens, closes, or is at rest.

Based on the earlier analysis of Mönch and Herminghas[30] and Shenay and Sharma,[29,31] we present a simple analysis of the situation using Figure 7, where a rigid glass plate is used, instead of a flexible one. A thin elastic film on a rigid substrate is subjected to forces of adhesion on its surface when it is brought into contact with the rigid plate. The distance-dependent attractive forces (e.g., van der Waals forces) lead to undulations, whereas the elastic force in the film provides stability. The figure shows the sinusoidal deformation, $u_2 = u_0 \sin(2\pi x_1/\lambda)$, of the film

(44) Lord Rayleigh. *Proc. London Math. Soc.* **1878**, *10*, 4.

at the interface, where λ is the characteristic length scale of the undulations. At location A, the film is subjected to the van der Waals force $A/6\pi(d - u_0)^3$ and the elastic force Eu_0/h, resulting in the net destabilizing force $F_A \approx A/6\pi(d - u_0)^3 - Eu_0/h$, where A is the effective Hamaker constant. Similarly, the net stabilizing force at B is $F_B \approx A/6\pi(d + u_0)^3 + Eu_0/h$. Instability ensues when $F_A \geq F_B$. In a linear approximation, Shenoy et al.[31] deduced the exact condition for the onset of instability in this setting as $A/6\pi d^4 \geq 2E/3h$. Because E/h has units of force (spring constant) per unit area [(N/m²)/m], the inequality signifies that instability ensues when the spring constant of the van der Waals forces ($A/6\pi d^4$) exceeds that of the elastic film ($2E/3h$).

The problem can be further analyzed under plane strain approximations ($\epsilon_{33} = 0$), which results in the following set of stress equilibrium relations in terms of the pressure field p and the displacement components $u_1(x_1,x_2)$ and u_2-(x_1,x_2)

$$-\frac{\partial p}{\partial x_1} + \frac{E}{3}\nabla^2 u_1(x_1,x_2) = 0$$
$$-\frac{\partial p}{\partial x_2} + \frac{E}{3}\nabla^2 u_2(x_1,x_2) = 0 \tag{2a}$$

and the incompressibility condition

$$\frac{\partial u_1(x_1,x_2)}{\partial x_1} + \frac{\partial u_2(x_1,x_2)}{\partial x_2} = 0 \tag{2b}$$

The right-hand side of eq 2a is 0, because the film is not subjected to any body forces. Equation 2 is solved using the vanishing displacement condition at the film–substrate interface, i.e., $u_1(x_1,x_2=0) = u_2(x_1,x_2=0) = 0$ and the condition of no slippage of the film over the rigid cover plate $u_1(x_1,x_2=h) = 0$. The fourth boundary condition is obtained by equating the pressure at the surface of the film to the traction due to van der Waals forces. Thus, using a linear approximation, the pressure, p, at $x_2 = h$ is written as

$$p = -\frac{A}{6\pi d^3}\left(1 + \frac{3u_2(x_1,x_2=h)}{d}\right) \tag{3}$$

For a thin film, eqs 2 can be simplified by using the lubrication approximation so that the terms containing $h\partial/\partial x$ are neglected. Integration of the simplified equations leads to following expressions for the displacements

$$u_1(x_1,x_2) = -\frac{3}{2E}\frac{dp}{dx_1}(hx_2 - x_2^2)$$
$$u_2(x_1,x_2) = \frac{3}{2E}\frac{d^2p}{dx_1^2}\left(\frac{hx_2^2}{2} - \frac{x_2^3}{3}\right) \tag{4}$$

where the pressure p remains independent of the thickness coordinate. Hence, at $x_2 = h$, the displacement $u_2(x_1,x_2=h)$ is obtained as

$$u_2 = \frac{3}{2E}\frac{d^2p}{dx_1^2}\frac{h^3}{6}$$

Inserting the expression for p (eq 3) into this relation, the following wave equation is obtained

$$\frac{d^2 u_2}{dx_1^2} + \frac{2}{h^2}\left(\frac{2E/3h}{A/6\pi d^4}\right)u_2 = 0 \qquad (5)$$

However, in a linear approximation, the instability condition suggests that the van der Waals spring constant scales linearly with the elastic spring constant of the film, i.e., $A/6\pi d^4 \sim 2E/3h$. Thus, eq 5 simplifies to

$$\frac{d^2 u_2}{dx_1^2} + \frac{2 u_2}{h^2} = 0 \qquad (6)$$

Equation 6 has a solution of the form

$$u_2 = u_{20}\sin\left(\frac{2\pi}{\lambda}x_1\right)$$

which signifies surface waves of wavelength $\lambda = \sqrt{2}\pi h = 4.44h$. Although the numerical coefficient does not have much significance in this approximate analysis, the linear scaling suggests that the length scale of the instability should depend only on the thickness of the film, not on any other material properties of the system. Furthermore, in the linear approximation, the discussion holds for any type of distance-dependent intermolecular forces. Shenoy and Sharma[31] did a more elaborate analysis of the problem and obtained the relation $\lambda = 3h$. The theoretical result was verified in the experiments of Mönch et al.[30] for a similar geometry. Experiments in Figures 1 and 2 are, however, more akin to the classical peel experiment. Understanding one-dimensional waves in this geometry calls for relaxation of the plane strain approximation, the incorporation of the bending of the flexible plate, and a stability analysis of the 3-D stress equilibrium relation. Work in this direction is in progress by Shenoy et al. (personal communication). Whereas the above analysis describes a scenario in which two surfaces are brought into contact, similar situation also arises when they are taken apart. Fluctuations inherent in the interface (e.g., thermal fluctuations, roughness of surfaces, fluctuations in material properties) can result in spatial variations in the adhesion forces. The resultant perturbations on the surface grow when a negative stress is applied, leading to nonuniform surface deformations.

   Amplitude. The length of the fingers or the amplitude is another morphological feature of the waves that is strongly influenced by the detailed energetics of the system. Experiments depicted in Figure 1 with films of different thicknesses and shear moduli and cover plates
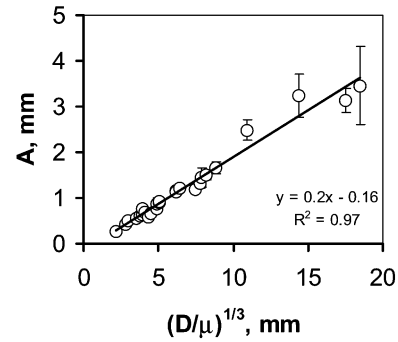

Figure 8. Amplitude (A) of the instability patterns in the geometry of Figure 1 obtained for films of different thicknesses and shear moduli in contact with cover plates of different rigidities. The amplitude is plotted as a function of the length scale $(D/\mu)^{1/3}$.
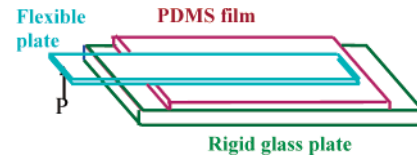

Figure 9. Schematic of the experiments in which a flexible cover plate is brought into contact with the film, and a very small load is applied to initiate a crack. The elastic film remains attached to the rigid glass plate. Crack initiation starts with the nucleation of uniformly spaced bubbles very close to the contact line.

of different flexural rigidities indicate that the amplitude increases with the flexural rigidity (D) of the cover plate and decreases with the shear modulus of the film. When the amplitude data obtained from different experiments are plotted against the quantity $(D/\mu)^{1/3}$, a linear relation is observed (Figure 8). Thus, the dependence of the amplitude on the flexural rigidity of the plates and the shear modulus is very similar to that of the critical thickness, h_c, on these parameters.

   Cavitation. The phenomenon of bubble formation in Figure 4 is further studied in two different experiments in the geometries of Figures 9 and 11. In experiments of the type depicted in Figure 9, a flexible plate is first brought into complete contact with the film and then a small force is applied to it to initiate a crack. Here, too, films of different shear moduli (μ) and thicknesses (h) were used with plates of different flexural rigidities (D). For thinner films ($h < h_c$), crack initiation is preceded by the formation of bubbles of uniform size very close to the contact line, as shown in Figure 10. Micrographs 10a–d show the
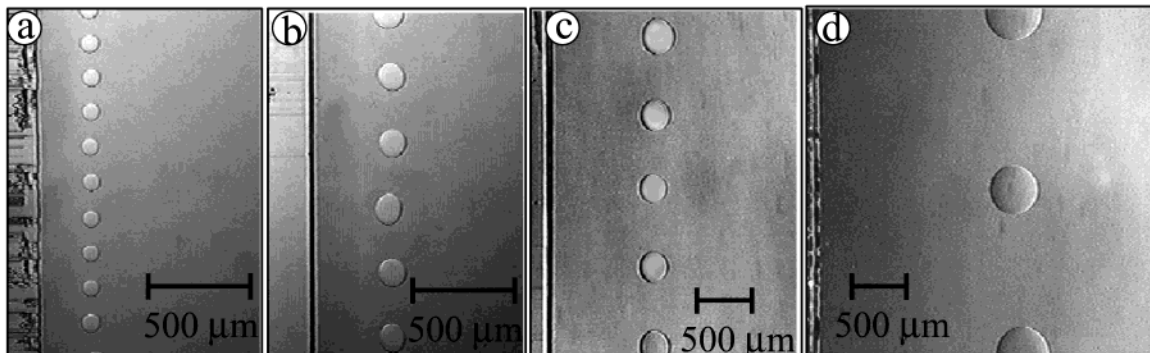

Figure 10. Video micrographs of bubbles formed close to the contact line in the experiments depicted in Figure 7. Bubbles of uniform size appear with uniform spacing, which remains independent of all material parameters, except the thickness of the film. The spacing follows the same law, $\lambda = 4h$. Micrographs a–d correspond to films of shear modulus $\mu = 1.0$ MPa and thicknesses $h = 40, 80, 190,$ and 360 μm, respectively. A flexible plate of rigidity $D = 0.02$ N·m was used with the films in micrographs a–c, and one of rigidity $D = 0.2$ N·m was used with the film in micrograph d.
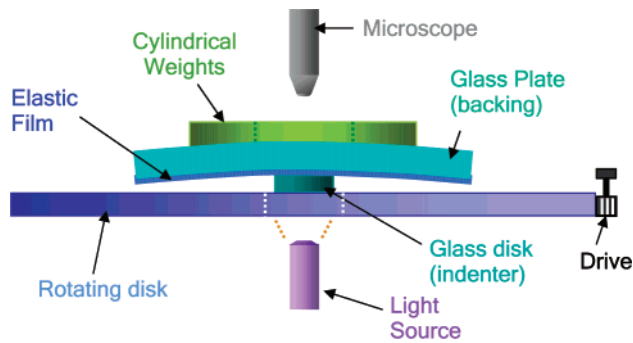
Figure 11. Schematic of the experiments in which an elastic film on a glass backing is brought into contact with a glass disk bonded to a rotatable frame. Debonding and bonding of the film is carried out using dead weights in the shape of annular rings.

patterns of bubbles for films of increasing thickness (40−360 μm) and of identical shear modulus ($\mu = 1.0$ MPa). In all of these cases, the bubbles appear much earlier than the actual opening of the crack, and they remain uniformly

spaced, with a spacing (λ) that follows the same relation to the thickness of the film, i.e., $\lambda = 4h$.

The experiments depicted in Figure 11 provide more insight into the process of cavitation or bubble formation at the interface of a confined thin elastic film and a rigid glass disk. The disk is kept fixed on a rigid support, and a thin elastic film on a flexible glass plate is brought into or out of contact with it from above. Debonding and bonding of the film are achieved by placing annular dead weights on the flexible glass backing, causing it to bend to a finite radius of curvature under the load. Evolving patterns of cavities or instabilities are formed at the interface during loading and unloading of the film. By loading, in this paper, we imply loading of the glass backing with dead weights, leading to detachment of the film from the indenter, and by unloading, we mean removal of these weights.

The video micrographs in Figure 12 show typical patterns of bubble formed during a loading and unloading cycle. In this particular experiment, an elastic film of thickness $h = 60$ μm and shear modulus $\mu = 0.9$ MPa remains strongly attached to a glass plate (50×50 mm)
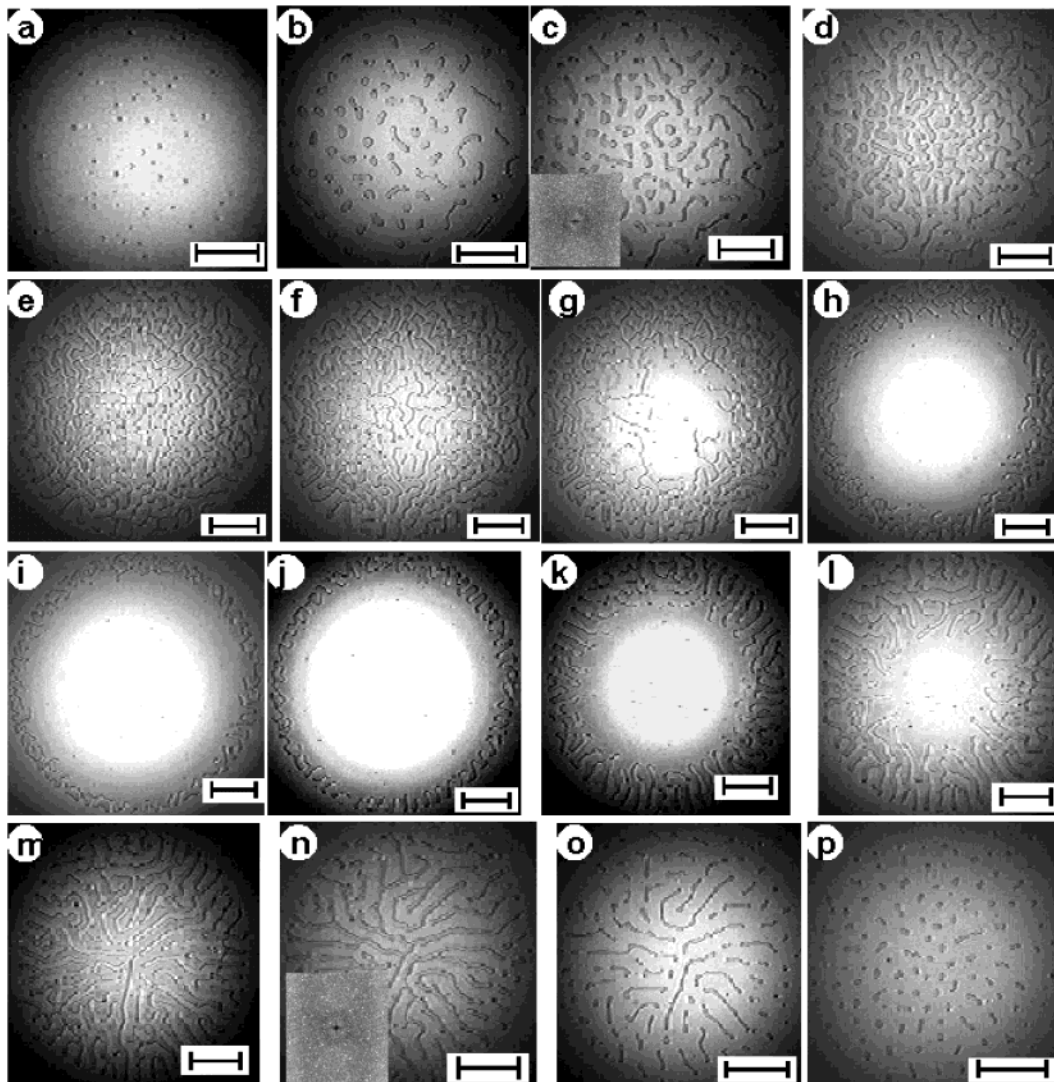

Figure 12. Video micrographs of cavitation patterns during loading and unloading obtained from the experiment described in Figure 11. A film of thickness $h = 60$ μm and of shear modulus $\mu = 0.9$ MPa remains strongly attached to a glass plate of flexural rigidity $D = 1.2$ N·m and is brought into contact with a glass disk coated with a HC SAM. As a load is applied, the film detaches from the disk, with the formation of bubbles or cavities. Micrographs a−i corresponds to nondimensional loads F_n (see text) = 0, 0.05, 0.07, 0.1, 0.18, 0.19, 0.25, 0.4, and 0.6, respectively, and j−p correspond to F_n = 0.3, 0.16, 0.1, 0.09, 0.04 0.013, and 0, respectively. The insets in a few micrographs indicate FFTs of the corresponding images. The horizontal line in each micrograph represents a length of 1 mm.

of flexural rigidity $D = 1.2$ N·m that is brought into contact with a glass disk of diameter $d_d = 8$ mm. The disk is coated with a monomolecular layer of hexadecyl trichlorosilane molecules to eliminate secondary interactions at the interface. The load is increased in steps of ~50 g by placing weights whose inner (d_i) and outer (d_o) diameters are 30 and 60 mm, respectively. The load is thus applied along a ring of diameter $d_a = {}^2\!/_3(d_o^2 + d_o d_i + d_i^2)/(d_o + d_i) = 47$ mm. An equivalent situation can be considered where the flexible plate is supported only on a disk without any contacting elastic film in between. The radial variation of the displacement of the flexible plate in that case can be deduced,[34] and the maximum displacement at the center can be expressed as $\epsilon_{max}/d_a = (P d_a/D) \times \eta^2[1 - \ln(\eta)]/8\pi$, where $\eta = d_d/d_a$ and P is the applied load. Whereas ϵ_{max}/d_a is a measure of aspect ratio of the gap between the two plates, the nondimensional quantity $P d_a/D$ signifies how much moment ($P d_a$) is applied with respect to the rigidity (D) of the flexible member. Therefore, the load data can be expressed in terms of the dimensionless quantity $F_n = P d_a/D$, making it independent of the rigidity D.

Different phases of bubble formation can be identified in Figure 12. At the beginning of the experiment the film remains in complete contact with the disk. The few scattered bubbles that appear at zero load (Figure 12a) are due to local imperfections and bending of the glass plate because of its own weight. As the load is increased from 0 to 0.07 (Figure 12a–c), the glass plate bends further, leading to an increased number of bubbles at the interface. Initially (Figure 12a,b), bubbles appear in a random manner and fast Fourier transforms (FFTs) of these micrographs do not indicate the existence of any dominant wave vector. A characteristic separation distance (λ) between the bubbles emerges, however, as the load is increased to $F_n = 0.07$ (Figure 12c). This distance (λ) decreases with increasing load as a result of the appearance of more bubbles at increased load. This is the bubble nucleation phase.

As the load is increased further, the number of bubbles saturates, and no new bubbles are formed. This is the bubble growth phase, during which bubbles grow in size with increasing load [$F_n = 0.1$ (Figure 12d) to 0.18 (Figure 12e)]. The radial separation between the bubbles, however, remains unchanged. FFTs of these images show a circular ring, signifying an isotropic instability pattern and a constant wave vector.

With increasing load ($F_n = 0.18$–0.19), bubbles start to coalesce, giving rise to interconnected patterns (Figure 12e and f) with thin filaments of contacted regions left between the bubbles. Coalescence of bubbles occur more toward the center, where the displacement of the plate is greatest. Complete detachment of the film, however, does not occur until a sufficiently high load (>0.25) is applied. At this load, the film loses contact with the disk, resulting in a circular debonded region (Figure 12g). This is the bubble coalescence phase.

With increased load (0.4–0.6), the central detached area grows in radius (Figure 12h and i), and fingerlike structures start to appear toward the circumference. The inter-connected pattern of instabilities is replaced by equally spaced fingers along the periphery of the detached region, thus forming the unidirectional (or 1-D) instability pattern characteristic of the peel geometry. The transition from the isotropic pattern in micrograph 12f to the 1-D pattern in micrograph 12g does not occur smoothly, however. Rather, it occurs abruptly as the load on the plate is increased. In fact, the transition to the 1-D pattern in Figure 11g can occur at a lower load if the glass plate is knocked even slightly. In other word, in micrographs
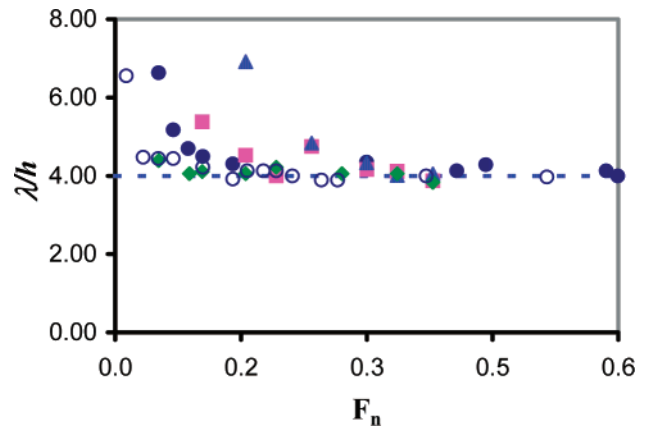

Figure 13. Characteristic separation distance between bubbles (in Figure 12) plotted as a function of load for films of different thicknesses. Symbols ◆, ●, ■, and ▲ represent data obtained during loading of the films of shear modulus $\mu = 0.9$ MPa and thicknesses $h = 36$, 60, 80, and 120 μm, respectively. Symbol ○ represents the unloading cycle for a film of thickness $h = 60$ μm and shear modulus $\mu = 0.9$ MPa. The figure shows that, in the bubble nucleation phase, the wavelength of the instability decreases from a higher value ($\lambda/h > 4$), but as the pattern of instability develops fully, λ/h decreases to ~4 and remains unaltered irrespective of the film thickness.

12e and f, the interface appears to be locked into a metastable state from which it jumps into a more stable state (Figure 12g) when perturbed. The pattern remains frozen in this state as the load is further increased, although the length of the fingers decreases.

The wavelength of the micrographs in Figure 12 is measured by FFT analysis of the images (for the isotropic pattern) and by estimating the peak-to-peak distance between the fingers (for the 1-D pattern). The wavelength (λ) data for films of different thicknesses ($h = 36$, 60, 80, and 120 μm) are plotted (solid symbols) with respect to the load applied in Figure 13. For films of all thicknesses, λ/h remains large (>4) at the beginning of the bubble nucleation phase; however, it decreases to 4 as the bubbles grow in number and size and then coalesce to form 1-D fingers. Similar results were obtained for films with different elastic moduli.

Instability patterns during unloading of the plate are shown in micrographs 12j–p. These patterns look quite different from the ones observed during loading. As the loads are withdrawn from the plate, the length of the fingers grows inward. Eventually, all fingers collapse at the center, as observed in micrograph 12m ($F_n = 0.087$). The patterns remain one-dimensional and do not go back to the isotropic forms as in micrographs 12a–f. The one-dimensional character of the patterns remains unaltered even at lower load (0.09 0.013), where cavities in the form of long fingers span from the center to the circumference of the detached area and the fingers simply grow thinner (Figure 12m–o). At zero load (Figure 12p) on the plate, the fingers break into bubbles, which look very similar to the classical Rayliegh–Kelvin instability[44] of a liquid jet or cylindrical liquid column. A similar phenomenon of the breaking up of a long cylindrical bubble into spherical bubbles was also observed in the experiments of Shull et al. (personal communication). The wavelengths of the instability patterns are estimated by analyzing the FFT spectra of the images or by the direct measurement of the separations between the fingers and are plotted in Figure 13. The open circles in this figure indicate the data obtained from a 60-μm film of shear modulus $\mu = 0.9$ MPa. The figure shows that the wavelength remains close to $4h$ for
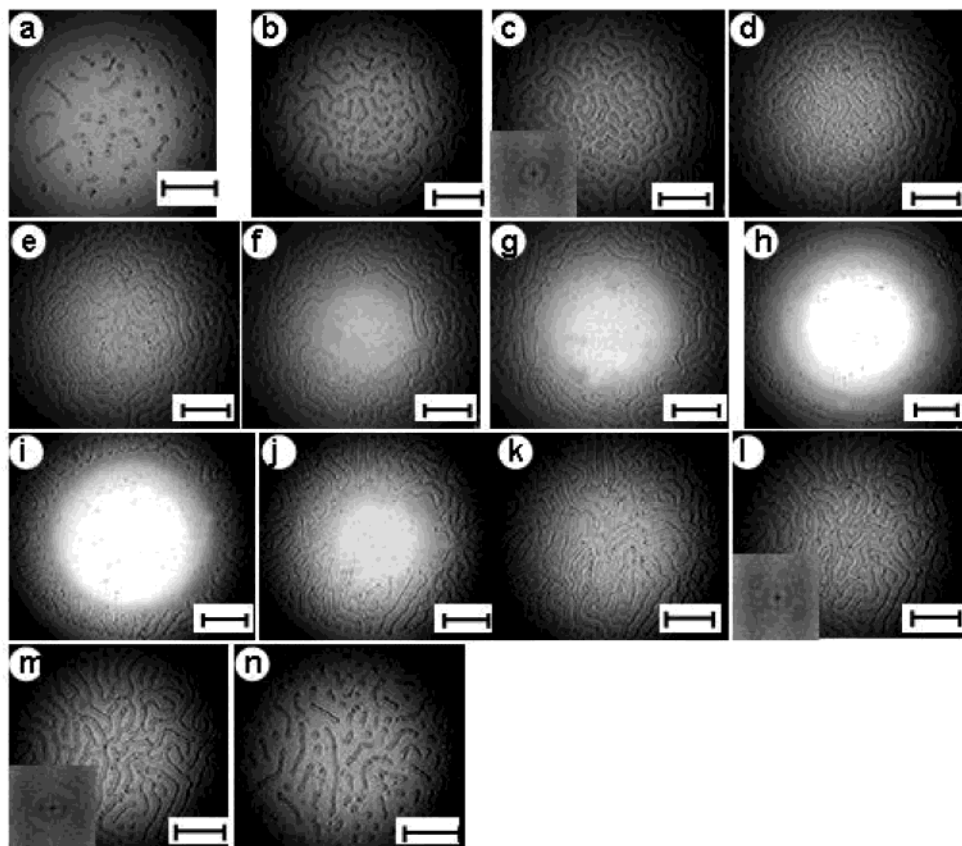
Figure 14. Video micrographs of cavitation patterns in loading and unloading experiments with a glass disk coated with PDMS molecules. The experiment is done on a film of thickness $h = 52$ μm and shear modulus $\mu = 0.9$ MPa. Micrographs a–h represent the loading cycle (0.07, 0.11, 0.14, 0.18, 0.21, 0.25, 0.28, and 0.46, respectively), and micrographs i–n represent the unloading cycle (0.32, 0.25, 0.21, 0.14, 0.11, and 0.07, respectively).

all loads, except very small ones for which the characteristic spacing between bubbles increases.

To summarize, the patterns are interconnected and isotropic during the loading phase, but they are radial or one-dimensional during the unloading phase. The characteristic length scales of the instability patterns during loading and unloading, however, remain similar. Interestingly, the 1-D pattern during unloading remains unaltered even during subsequent loading and unloading cycles. This observation was made in experiments in which the glass plate was first loaded, then unloaded to an intermediate weight (not zero load), and then loaded again. The patterns did not evolve as in micrographs 12a–i; rather, they retrace the path in Figure 12j–p.

What causes this hysteresis and irreversibility in pattern formation? JKR-type contact mechanics experiments on the glass disk showed that there is negligible adhesion hysteresis (2 mJ/m²) between the PDMS elastomer and the HC SAM on the glass, suggesting that hysteresis in pattern formation does not stem from adhesion hysteresis on the surface. However, there can be hysteresis due to the interfacial friction if shear stress develops at the interface as a result of the mismatch of the moduli[45] of the polymer film and the glass contactor. The shear stress, however, can be released if the interface has low friction, thus allowing for interfacial slippage.[15] To test this hypothesis, loading and unloading experiments depicted in Figure 11 were conducted on a surface grafted with poly(dimethylsiloxane) (PDMS) polymer, which also exhibits very low adhesion hysteresis ($\sim$2 mJ/m²) but

which provides lower resistance to slippage than HC-coated surfaces.[15,46]

Experiments on the PDMS-coated surface led to different observations, which are summarized in the evolution patterns in Figure 14. Video micrographs a–h and i–n in this figure represent the loading and unloading cycles, respectively. Whereas, during loading, the patterns observed with the PDMS- and HC-coated surfaces look similar, the patterns are different during unloading. As the load is decreased from $F_n = 0.46$, 1-D fingers are initially formed, but they do not grow long toward the center, unlike the case with the HC-coated surface. With decreasing load, interconnected isotropic cavitation patterns characteristic of the loading cycle emerge, signifying reversibility of the evolution path. Furthermore, micrographs 14e and f during loading and 14j and k during unloading indicate that detachment and reattachment of the central region of the film with the disk occur at similar loads, unlike the case for the HC-coated disks. It is plausible that high interfacial slippage at the interface of the PDMS film and the PDMS-grafted glass disk releases the interfacial shear stress and thus eliminates the hysteresis in pattern formation during loading and unloading cycles.

Pattern Formation under Rotation. The phenomenon of pattern formation was further studied by applying rotational shear to the film relative to the contacting disk. In these experiments, a rigid glass indenter fixed at the center of a supporting disk was rotated (0.5–5 rpm) by a drive with respect to the elastic film. Figure 15 shows the

(45) Hutchinson, J. W.; Suo, Z. *Adv. Appl. Mech.* **1991**, *29*, 63.

(46) Zhang Newby, B.-m.; Chaudhury, M. K. *Langmuir* **1998**, *14*(17), 4865.
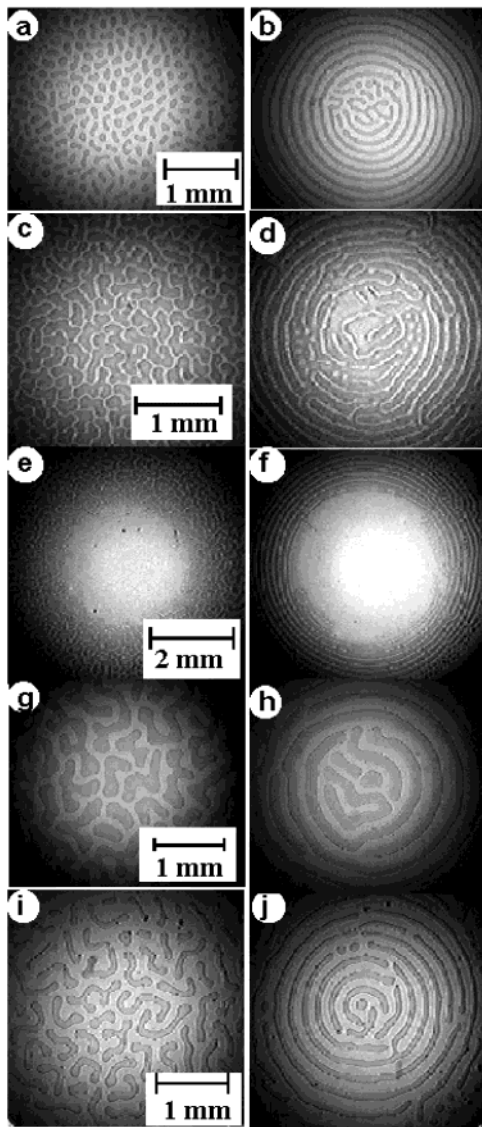
Figure 15. Video micrographs of cavitation patterns with films of different thicknesses and under different normal loads and rotational shears. Micrographs a–h and i,j represent films in contact with glass disks coated with a HC SAM and PDMS chains, respectively. The isotropic instability pattern in micrograph a corresponds to a film of thickness $h = 36$ μm and shear modulus $\mu = 0.9$ MPa, subjected to a load of $F_n = 0.05$ in the geometry of experiment in Figure 11; the bubbles coalesce into concentric rings (b) when a rotational shear is applied at the interface. Similarly, micrographs c,d and e,f were obtained for the same film subjected to nondimensional loads 0.11 and 0.16, respectively. Micrographs g and h were obtained for a film of thickness $h = 80$ μm and shear modulus $\mu = 0.9$ MPa subjected to load 0.16. Micrographs i and j represent the patterns obtained for a film of thickness 52 μm and elastic modulus μ = 0.9 MPa under a load of 0.14 in contact with a PDMS-grafted glass disk.

cavitation patterns obtained for films of thickness $h =$ 36, 52 and 80 μm and shear modulus $\mu = 0.9$ MPa. The pattern in micrograph 15a is obtained for the 36-μm film under load $F_n = 0.05$. This pattern is akin to that obtained for a 60-μm film in the loading cycle (Figure 12) under similar loading conditions. The pattern changes dramatically (Figure 15b), however, when a shear is applied by rotating the contacting disk relative to the film. The bubbles collapse together to form equally spaced concentric rings, which remain stable with respect to the rotational speed of the disk. The pattern does not change even after the cessation of rotation. Whereas, at lower loads, rings appear
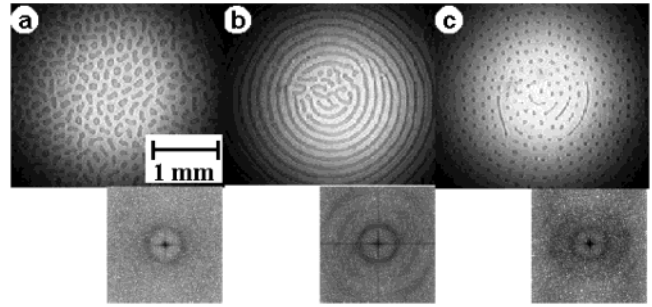

Figure 16. Video micrographs show how the cavitation patterns evolve as (a) a load is applied, (b) the interface is subjected to rotational shear, and (c) the load is withdrawn. The patterns correspond to a film of thickness $h = 36$ μm and shear modulus $\mu = 0.9$ MPa. The applied load is $F_n = 0.05$. The figure also shows the corresponding FFT spectra of the images.
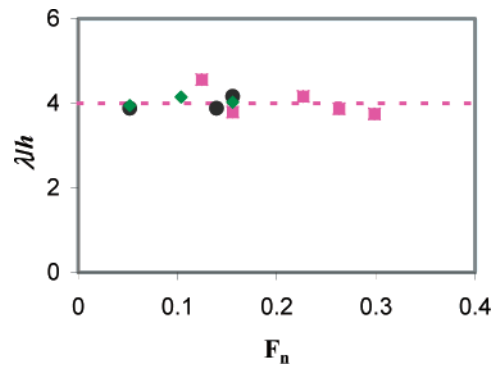

Figure 17. Characteristic separation distance between the rings or bubbles (in Figure 13) plotted as a function of load for films of different thicknesses. Symbols ◆, ●, and ■ indicate films of shear modulus $\mu = 0.9$ MPa and thicknesses $h = 36$, 60, and 80 μm, respectively. The figure shows that the λ/h value for all thicknesses remains close to 4.

throughout the contact area, at higher loads (e.g., Figure 15c,d and e,f at $F_n = 0.11$ and 0.16, respectively) the bubbles tend to coalesce toward the center of the contact area, and a circular debonded region forms; away from the center, stable concentric rings appear that remain equally spaced. A similar phenomenon was observed for films of higher thicknesses (e.g., Figure 15g,h for a film with a thickness of 80 μm) and also with the PDMS-grafted glass disk (Figure 15i,j).

The evolution of the instability patterns is summarized in Figure 16. A film of thickness $h = 36$ μm and shear modulus $\mu = 0.9$ MPa in contact with a HC-coated surface is subjected to nondimensional load $F_n = 0.05$, which results in micrograph 16a. When a rotational shear is applied, the pattern transforms to the concentric equally spaced rings shown in Figure 16b. The rings remain unaltered when the rotational shear is withdrawn. As the normal load is withdrawn, the rings break up into bubbles in the same way as shown in Figure 12p.

Figure 17 shows the characteristic separation distance (λ) between the rings as estimated by measuring the spacing between the rings, as well as by analyzing the FFT spectra of the images. Data from experiments with films of different thicknesses and of shear modulus $\mu = 0.9$ MPa are plotted as a function of load on the plate. λ/h is again found to be ~4 for different cases.

The rings in Figures 15 and 16 are similar to curvilinear vortex patterns, which have been observed in the viscometric flow of a viscoelastic liquid between two parallel plates.[10,47] Above a critical Deborah number, these vortices propagate in the form of concentric spirals from a lower

to a higher critical radial position between the plates. Interestingly, in that case also, the radial wavenumber scales linearly with the gap (h) between the plates and also depends on the ratio of the rheological properties of the viscoelastic liquid. The driving forces of the instabilities, however, are different in the two situations. In viscometric flow, the vortices are formed because of stress-induced secondary radial flow over and above the base torsional flow. In the case of thin elastic films, the driving force is the interfacial-shear-induced coalescence of bubbles.

Questions arise as to where the bubbles originate during cavitation experiments. In this context, the experimental and theoretical works of Gent et al.,[17−19] Lindsey,[24] and Pond[21] on cavitation at the interior of a rubber block are worth reviewing. The essence of their understanding is that cross-linked rubber contains microscopic air bubbles ($\sim$10 Å to 1 μm) that inflate when sufficient negative pressure is applied. The critical negative pressure decreases as the initial size of bubbles increases, reaching a lower limit of $5\mu/2$, which corresponds to a bubble size on the order of 0.1 μm. These bubbles are still smaller than the visible range. Air can also be present in rubber in a dissolved state so that the vapor pressure of air in the rubber is equal to its partial pressure in the cavities. This dissolved air can diffuse from the bulk into the cavities when a negative pressure is applied. A similar situation can also occur in the case of bubble formation at the interface of an elastomer and glass. The intrinsic roughness of the interface could host trapped air bubbles, which appear when the two surfaces are separated. However, the bubbles cannot appear randomly, because the distance-dependent attractive forces at the interface and the consequent response of the elastic film give rise to these stress patterns, so that the spatial positions of the bubbles are determined even before the bubbles become visible. Therefore, although the defects at the interface could take part in the formation of bubbles, it is the intrinsic balance of the forces in the film that determines the spacing between the bubbles or the fingers. It is not clear yet, however, how shear helps in the coalescence of bubbles and the subsequent formation of concentric rings in the rotation experiment.

Summarizing Comments

The experiments reported herein indicate that surface of a confined thin elastic film subjected to adhesion forces undergoes undulations leading to different kinds of instability patterns depending on the geometry of the experiment. In the geometry of the peel experiment, two different length scales are identified: the thickness of the film, h, and the ratio of the material properties of the flexible contactor and the film, $(D/\mu)^{1/3}$. Whereas h solely

determines the characteristic length scale of the waves, i.e., λ, the amplitude of waves, A, is determined by $(D/\mu)^{1/3}$. In experiments with infinitely rigid plate ($D \to \infty$),[30] isotropic instability patterns are observed that are characterized by a single length scale, i.e., the distance λ between the surface waves. λ remains independent of the nature of the surface force that triggers the instability because the intrinsic balance of forces within the layer remains independent of the surface force, which enters as a boundary condition. Problems of this kind are different from those in which the instability is triggered by a body force. Examples of this latter kind of instability are the intermolecular-force-induced spinodal dewetting[48,49] of an ultrathin (<100 nm) liquid film and the electric-field-induced hydrodynamic instabilities[50] in a dielectric polymer layer between two parallel plates (capacitors). In either case, the body force appears in the equations representing the force balance within the layer, and the length scale of the instability depends on the ratio of the surface tension forces to the gradient of the body force, in addition to the thickness of the film (h). The absence of a body force in the problem discussed in this paper makes λ depend only on h. The invariability of λ with the velocity of the moving contact line suggests that the fingering phenomenon occurring during the peeling of a viscoelastic adhesive could be due to the elastic character of the adhesive. The uniform morphology of the patterns in purely elastic systems is also useful for understanding viscoelastic systems. For example, branching in viscoelastic fingering occurs in a systematic manner at right angles to the crack and behind the crack tips.[11] This is in contrast to viscous fingering, where branching occurs by tip splitting[5,6] and at angles less than 90°. Although the instability patterns of these two systems are quite distinguishable visually and also by fractal analysis, the patterns of purely elastic systems (Figures 3 and 4) could serve as definitive evidence of the role of elastic instability in a viscoelastic system.

(47) Öztakin, A.; Brown, R. A. *J. Fluid Mech.* **1993**, *255*, 473.

(48) Reiter, G. *Langmuir* **1993**, *9*, 1344.
(49) Khanna, R.; Sharma, A. *J. Colloid Interface Sci.* **1997**, *195*, 42.
(50) Schaffer, E.; Thurn-Albrecht, T.; Russell, T. P.; Steiner, U. *Nature* **2000**, *403*, 874.